Pol. J. Environ. Stud. Vol. 32, No. 1 (2023), 341-351
DOI: *10.15244/pjoes/153928* ONLINE PUBLICATION DATE: 2022-12-05

Original Research

Forest Terrain Inversion Based on Icesat-2/ATLAS with Different Laser Intensities

Lei Xi, Linxia Li, Qingtai Shu*, Yang Sun, Jinjun Huang, Hanyue Song

College of Forestry, Southwest Forestry University, Kunming 650224, China

Received: 5 July 2022
Accepted: 8 September 2022

Abstract

There are various problems concerning the acquisition of forest digital terrain using satellite-based LiDAR (LiDAR). In this paper, a method for extracting the classified photon point cloud is summarised based on the photon point cloud acquired by ICESat-2/ATLAS strong and weak beams for forest digital terrain inversion. In this study, ATLAS was used as the data source to group canopy heights, and airborne LiDAR G-LiHT was used as the validation data to verify the effect of different canopy heights on the inversion of the understorey terrain. The results show that, when the canopy heights were not grouped, the inversion accuracy of both strong and weak ATLAS beams was higher, with an R^2 greater than 0.99, an RMSE of less than 0.7 m, and an MAE of less than 0.4 m. Overall, the strong beams were superior. Moreover, when the canopy heights were grouped, the R^2 was greater than 0.99 and the accuracy was best at the canopy height of 5-10 m. The R^2 decreased when the height exceeded 35 m. The inversion accuracy of both the strong and weak ATLAS beams was higher than 0.99. The accuracy of both strong and weak beam inversions was extremely high, with the strong beam being superior overall. However, both strong and weak beams can provide a scientific basis for the inversion of understory DTMs. Canopy height affected the inversion accuracy, which was inversely proportional to the canopy height, with an increase in canopy height causing a decrease in the accuracy. The inversion of the understorey topography was better than that of the dwarf tree and shrub layers.

Keywords: ICESat-2/ATLAS, digital ground model, photon point cloud, canopy height

Introduction

As the largest proportion of terrestrial ecosystems, terrestrial forest ecosystems have been the subject of much academic research, involving aspects such as canopy height [1], forest structure, and understorey topography. Large-scale and high-precision research and evaluation require remote sensing technology to provide large amounts of qualitative and quantitative data [2]. Satellite-based LiDAR has the advantage of both large-scale data acquisition and high accuracy in depicting vertical information. To date, four laser altimetry Earth observation satellites have been successfully launched worldwide: ICESat for the Geological Laser Altimeter System (GLAS) [3], ICESat-2 for the Advanced Terrain Laser Altimeter System (ATLAS) [4, 5], Gaofen-7 (GF-7), and the Global Ecosystem Dynamics Research Satellite (GEDRS) [6].

Photon counting radar systems perform excellently in the acquisition of vertical and horizontal structures,

*e-mail: shuqt@swfu.edu.cn

but relatively little research is focused on inverting understory DTMs in areas with large topographic relief and very high amounts of vegetation cover. In 2016, Amy L. Neuenschwander et al. [7] explored the performance characteristics and potential uncertainties associated with ICESat-2 vertical sampling errors, which included errors in perceived height values and measurement accuracy. In densely vegetated communities, topographic errors were shown to be between 1.93 m and 2.52 m and canopy errors between 0.28 m and 1.25 m. In 2019, Narine, Lana L. et al. used ATL08 data to examine the accuracy of ICESAT-2 sections in vegetated areas both horizontally and vertically in Finland and determined that horizontal deviations of less than 5 m fully satisfied the design accuracy of 6.5 m [8]. In 2020, Xing Yanqiu et al. used ATLAS multichannel data to assess the ability to estimate forest topography, and the results showed that ATLAS products performed well in the study area at all laser intensities and laser pointing angles. However, the ability to detect terrain under different canopy regimes was not discussed and was refined in this study [9]. In order to investigate whether the accuracy of ICESat-2/ATLAS products for inversion of forest understory topography with different laser intensities can be further improved under different canopy height conditions. We use small-spot airborne LiDAR as validation data to verify and discuss the ATL03 photon point cloud data after connecting it to the ATL08 product classification marker. We explore its ability to invert the understory terrain and further investigate the effect of canopy height on the inversion of understory terrain with different laser intensities.

The objectives of this study were: (1) to determine the capability of a satellite-borne photon-counting radar to detect terrain in a forest with very dense cover in a mountainous area at different laser intensities; (2) to analyze the ability of strong and weak beams to detect the forest understory terrain under different forest canopies; (3) to summarise and design a process-oriented procedure for processing ATLAS data.

Materials and Methods

Study Area

As shown in Fig. 1, the study area was Oxford County in western Maine, USA, at latitude and longitude of 70°13′17″W-71°7′35″W and 43°49′16″N-45°25′1″N. Oxford County is bordered by Canada to the north and New Hampshire to the west. The area under jurisdiction is 563400.1136 hm^2. The state is influenced by high latitudes and cold and warm Atlantic currents and is divided into three climatic zones. Oxford County is in the southern inland zone, with cool summers and cold, dry winters, and has 90% forest cover. The topography is undulating with an elevation range of 180 m to 1608 m. The forest canopy height range in the study area is 0.09 m to 34.80 m when the CHM is superimposed on the study area.

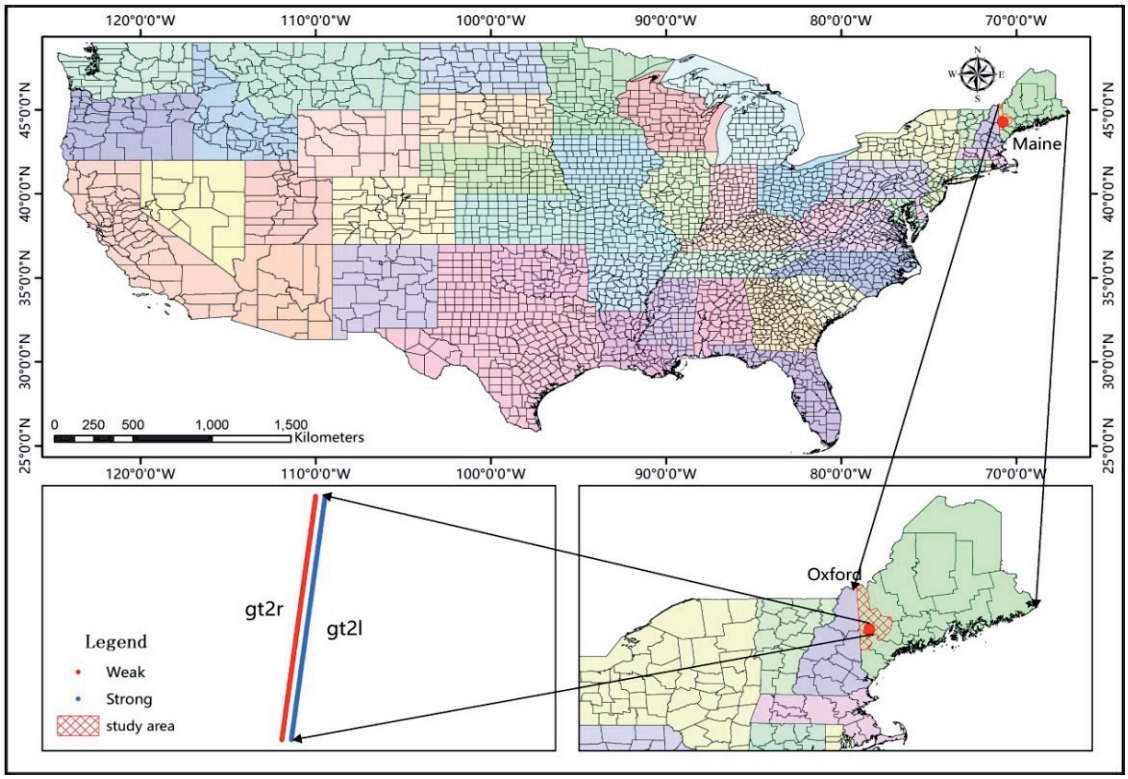

Fig. 1. Location of the study area.

ICESat-2 Data Products

The official NASA product descriptions for satellite 2 define 21 data products, grouped into 3 categories, named ATL01~ATL21 [10]. All data are stored in Hierarchical Data Format Version 5 (HDF5) and the data products used in the study were ATL03 (Global Geolocated Photon Data) and ATL08 (Land and Vegetation Height) [11].

The ATL03 data products include geospatial location information such as time, latitude, longitude, elevation, and geoid correction information for all photon events [12, 13]. Each photon is indexed to link all the hierarchical data, and there are two types of photon indexes in the ATLAS data. One is a segmentation along the track distance, i.e., a segment every 20 m, and each segment is identified by a unique 7-digit number, which is used to generate the segment classification index in ATL08 [14, 15]. The 7-digit segment name is stored in segment_id, and the identification number of the starting photon of each segment is stored in ph_index_beg [16]. The other type of numbering is based on the transmission time sequence of the photon signals, which are called photon data transmission time sequence numbers, and this type of data is recorded under the ATL03/gtx/heights file according to such sequence numbers.

The ATL08 data product is ATL03 data after indexing of the partitioned segments. The Differential, Regressive, and Gaussian Adaptive Nearest Neighbor (DRAGANN) algorithm was used to complete photon denoising, and then the photon point cloud classification algorithm was used. The photon point cloud was classified into four categories: noise, ground, canopy, and canopy top photons [17]. The classification results were recorded in classed_pc_flag in the form of segments. The study used ATL03_20190308012710_10630206_003_01.h5 and ATL08_20190308012710_10630206_003_01.h5 obtained on 8 March 2019, which involve orbital strong and weak beam numbers gt2l and gt2r. The data products are available on the official website for download (https://nsidc.org/data/icesat-2, accessed on 13 January 2022) [18].

G-LiHT Airborne Small Spot Lidar Data

The study data was selected from LiDAR data acquired by NASA in June 2015 using an airborne system (Goddard's LiDAR, Hyperspectral Thermal Image (G-LiHT)) and a Riegl (VQ-480) laser measurement system with a wavelength of 1550 nm, a pulse repetition rate of 150 kH_z, and a point cloud density of 10/m^2. The released products were a Canopy Height Model (CHM) and Digital Terrain Model (DTM) with a processed spatial resolution of 1 m [19]. The data were acquired in June 2015. The visualization website (https://openaltimetry.org, accessed on 13 January 2022) was used to query the selection of ICESat-2 data products that overlapped with the G-LiHT data. The G-LiHT data used were White_Mtns_Jun2015_l0s0_CHM.tif and White_Mtns_Jun2015_l0s0_DTM.tif, sourced from the NASA Goddard Space Flight Center website (https://glihtdata.gsfc.nasa.gov, accessed on 13 January 2022) [20].

ATL03 Products Associated with ATL08 Products

The ATL03 and ATL08 products with overlapping ICESat-2 satellite orbits in the study area were first correlated, and ground photons were obtained from the ATL03 photon data calibrated from the ATL08 single-photon data after photon classification. Then, they were calibrated for accuracy against the airborne DTM data [3, 16]. The study route is shown in Fig. 2 and the main steps are as follows:

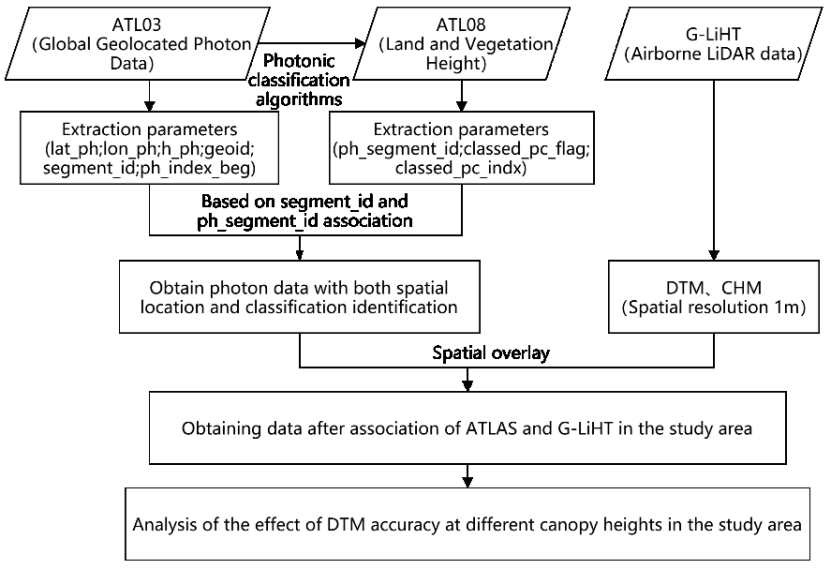

Fig. 2. Study flow chart.

1. The orbit locations were viewed on the ICESat-2 data visualisation website. And overlap between the ATLAS and G-LiHT trajectories was identified as the study area in conjunction with the range of airborne kml trajectories published by G-LiHT. The overlap of ATLAS products with G-LiHT's DTM and CHM data in the study area is shown in Fig. 3. In the figure, gt2r (weak) trajectories are shown in red, and gt2l (strong) trajectories are shown in blue.
2. The parameters in the ATL03 product are: photon segment number, photon segment start photon, latitude, longitude, elevation, and geoid correction information (segment_id, ph_index_beg, lat_ph, lon_ph, h_ph, geoid) [21, 22], respectively, based on code written in Python language on the Pycharm platform for batch extraction. The parameters in the ATL08 data are: photon segmentation information, single-photon classification identifier, and photon segmentation relative ordinate (ph_segment_id, classed_pc_flag, classed_pc_index). The parameters extracted for the study are shown in Table 1.
3. The zone number in the photon segment information extracted from ATL08 was used to correlate the photon zone number in ATL03, to match the same zone number in both data, and to obtain the starting photon sequence number and the photon segment relative sequence number in that zone grouping in the ATL08 data product. Moreover, the two can be summed to obtain the photon data transmission time sequence number in the ATL03 data product [4, 23]. The specific formula is classed_pc_index+ph_index_beg -1. Using this formula, the photon position information in the ATL03 product

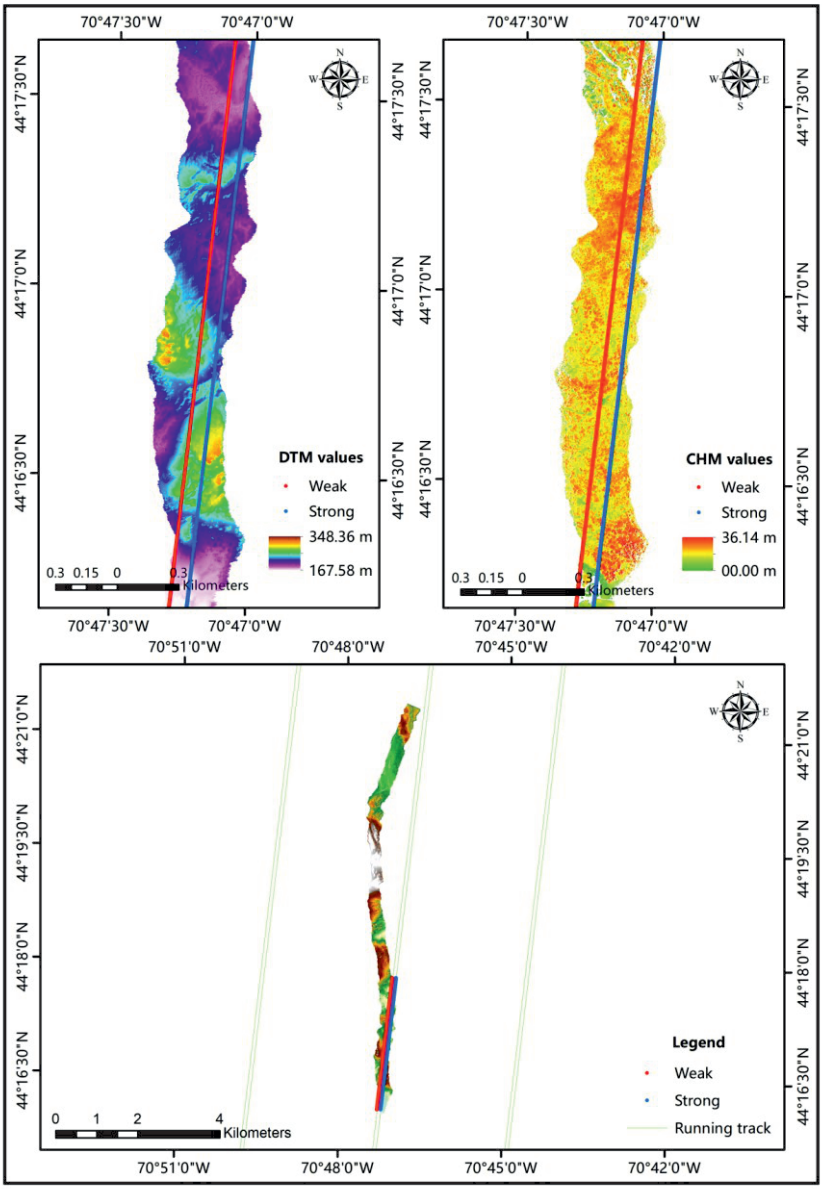

Fig. 3. Schematic representation of the overlap between the ATLAS orbit and the G-LiHT orbit.

Table 1. Parameters of the Advanced Laser Altimeter System (ICESat-2/ATLAS) used in the paper.

Name	Description	Path
lat_ph	Latitude of each received photon	ATL03/gtx/heights/lat_ph
lon_ph	Longitude of each received photon	ATL03/gtx/heights/lon_ph
h_ph	Height of each received photon	ATL03/gtx/heights/h_ph
geoid	Geoid height above WGS-84 reference ellipsoid [15].	ATL03/gtx/geophys_corr/ geoid
segment_id	A 7 digit number identifying the along-track geolocation segment number [42].	ATL03/gtx/geolocation/ segment_id
ph_index_beg	Index (1-based) within the photon-rate data of the first photon within this segment [31].	ATL03/gtx/geolocation/ ph_index_beg
classed_pc_flag	Land Vegetation ATBD classification flag for each photon as either noise, ground, canopy, and top of canopy. 0 = noise; 1 = ground; 2 = canopy; or 3 = top of canopy [15].	ATL08/gtx/signal_photons/ classed_pc_flag
classed_pc_indx	Index (1-based) of the ATL08 classified signal photon from the start of the ATL03 geolocation segment specified on the ATL08 product at the photon rate in the corresponding parameter, ph_segment_id [16].	ATL08/gtx/signal_photons/ classed_pc_indx
ph_segment_id	Segment ID of photons tracing back to specific 20 m segment_id on ATL03 [15].	ATL08/gtx/signal_photons/ ph_segment_id

can be correlated with the photon classification mark in the ATL08 product to obtain photon cloud data with both a classification and spatial position [12, 24].

4. The extracted classed_pc_flag is an official classification marker provided by NASA with a value domain of any integer in [0,3], and the markers are noise 0, ground 1, canopy 2, and canopy top 3 [25, 26]. In this study, we used all photons with a classification marker ground 1 as the forest ground photons (8487 and 2297 strong and weak beam ground photons, respectively). Fig. 4a) and 4b) corresponds to the ATLAS data strong and weak beam inversions of the understorey terrain profiles, respectively.
5. Using spatial superposition and concatenation, the extracted ground photons were derived and then compared with the DTM values of the airborne G-LiHT data for analysis. Finally, it was specified that photons with an absolute value of the difference between them greater than 20.8 m were misclassified photons and were removed. The strong and weak beam laser data were then fitted and inverted separately to remove outliers and nulls with residual absolute values greater than 1.80, resulting in a final strong and weak beam ground photon count of 7864 and 2168.
6. We investigated whether different canopy heights corresponding to different forest vegetation cover at different laser intensities had any effect on the accuracy of the DTM inversion in the forest understory. The canopy height stratification data were determined to be CHM data acquired by airborne G-LiHT. In 5 m segments, after removing outliers and nulls, the data were divided into seven groups by CHM, namely (0-5 m], (5-10], (10-15 m], (15-20 m], (20-25 m], (25-30 m] and (30-35 m]. The correlation evaluation metrics of the two lasers intensity inversion forest DTMs were counted in groups.

Accuracy Assessment Criteria

To evaluate the relationship between the inverse forest floor and airborne G-LiHT data at different laser intensities in the ATLAS data, the coefficient of determination (R^2), root mean square error (RMSE), and absolute mean error (MAE) at two laser intensities were separately statistically evaluated [11, 27–29]. To investigate the extent to which the vegetation canopy height and vegetation cover at different ATLAS laser intensities affected the accuracy of DTM inversions in the forest understory, we separately conducted inversions for different laser types within different canopy scales (zone groups), using the ATLAS ground photon elevations minus the corresponding elevations of airborne G-LiHT, and statistical indicators of errors by laser type (RMSE, R^2, MAE number, and weight of different canopy heights (N)) [30, 31]. The accuracy evaluation metrics used in the study are formulated as follows:

$$R^2 = 1 - \frac{\sum_{i=1}^{n} (y_i - \hat{y}_i)^2}{\sum_{i=1}^{n} (y_i - \bar{y})^2} \quad (1)$$

$$RMSE = \sqrt{\frac{\sum_{i=1}^{n} (y_i - \hat{y}_i)^2}{n-1}} \quad (2)$$

$$MAE = \frac{1}{n}\sum_{i=1}^{n} |(y_i - \hat{y}_i)| \quad (3)$$

where y_i is the actual value (m); $\hat{y}_i$ is the estimated value (m); $\bar{y}$ is the estimated mean value (m); and n is the number.

$$N = \frac{n}{N_{\text{Total}}} \times 100\% \quad (4)$$

where n is the number of photons in each canopy height segment; N_{total} is the total number of photons; and N is the ratio of the number of photons in each segment to the total number of photons.

Results and Discussion

Overall Inversion Accuracy of ATLAS with Different Laser Intensities

To investigate the accuracy of the inversion of the understorey DTM using ATLAS with different laser intensities, a table showing the accuracy of the strong and weak beam inversions was produced. Figure 5 shows scatter plots of strong and weak beam inversion of forested terrain profiles, plotted using the distance along the track as the horizontal coordinate and the height value of the forested terrain as the vertical coordinate (Fig. 4).

According to the scatter plot of 7864 strong-beam ground photons in Fig. 4a) and the corresponding G-LiHT validation data, the inversion results are in good agreement with the validation results, demonstrating that the strong-beam inversion results are superior to the 2168 weak-beam ground photon fits in Fig. 4b). In combination with the analysis of the effective number of strong and weak beam photons, it was found that the strong beam was more sensitive to detecting local details on the forest floor and the forest floor topography, especially when gully areas were present [9].

Based on the quantitative analysis of the study results in Table 2 and Fig. 5, where the R^2 of the strong and weak beam inversions of the understorey DTM were greater than 0.99, it was found that the inversion of the understorey DTM using ATLAS data was in general agreement with the validated DTM from the G-LiHT data. The results show that the performance and accuracy of the strong beam inversion of the understory DTM in this study were superior to that of the weak beam. This is because, when measuring the same type of object, the difference in laser emission intensity between the strong and weak beams is approximately four times. Thus, the strong beam can obtain more photon information than the weak beam; however, the mean values of R^2 = 0.99945, RMSE = 0.6466 m, and MAE = 0.3686 m for the strong and weak beams indicate that they can both adequately invert the forest DTM with a small error. The strong and weak beams can provide an accurate basis for the inversion of and represent a new means to investigate the forest DTM.

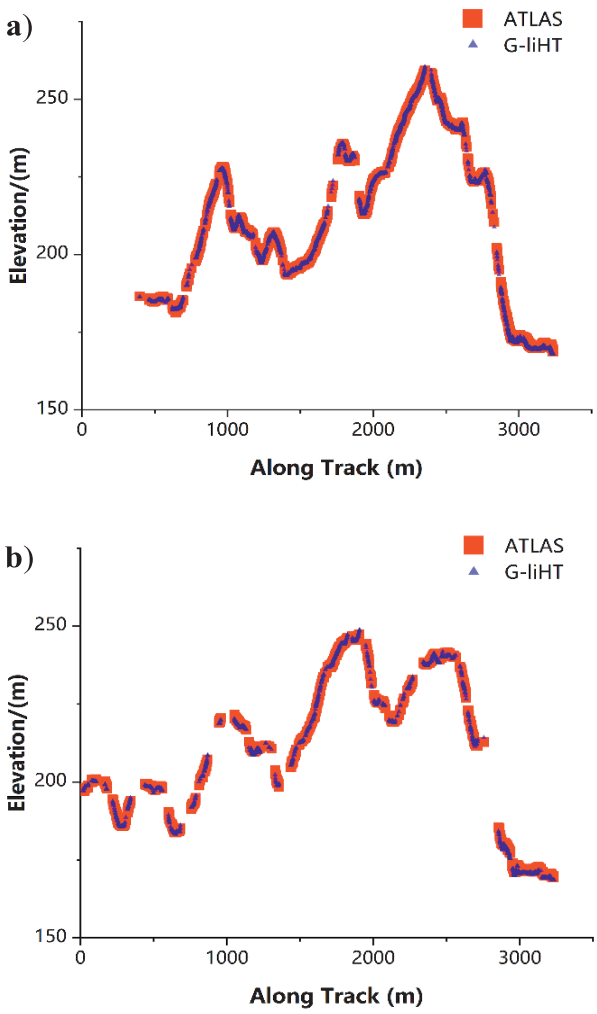

Fig. 4. a) Strong beam inversion of forested terrain profiles from ATLAS data. b) Weak beam inversion of forested terrain profiles from ATLAS data.

Analysis of the Impact of Different Canopy Scales

To investigate the accuracy of the inverse forest DTM for different vegetation canopy height and vegetation cover degree using different ATLAS laser intensities, the accuracy evaluation factors of seven groups of canopy scales using two laser types were calculated, as shown in Table 3. As the forest cover in the project area was very dense and the climate is cool in summer and cold and dry in winter, the forest canopy height range was 0 m-34.8 m; thus, in this study, we divided the CHM into seven groups with a 5 m interval for each height value, as shown in Table 3.

Table 2. Estimation accuracy statistics of ICESat-2/ATLAS data using different laser types.

Laser Type	Expressions	R^2	RMSE (m)	MAE (m)
Strong	$Y = -13.67 + 1.120X - 0.000262X^2$	0.9995	0.6348	0.3556
Weak	$Y = -12.12 + 1.102X - 0.000219X^2$	0.9994	0.6584	0.3816
Mean		0.99945	0.6466	0.3686

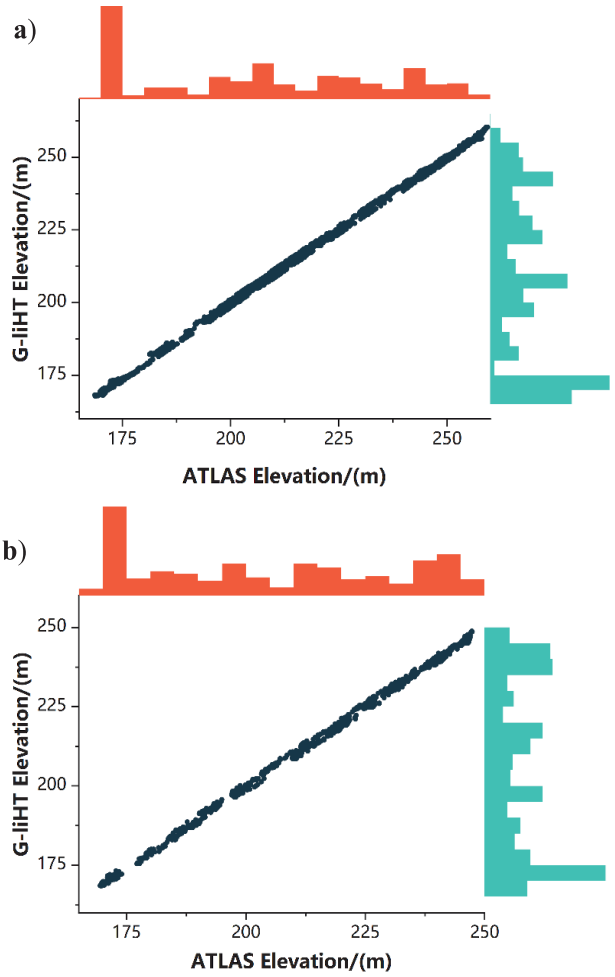

Fig. 5. a) Scatter plot of ATLAS and G-LiHT data using strong beams. b) Scatter plot of ATLAS and G-LiHT data using weak beams.

The number and weight of different canopy heights (N%) in Table 3 show that the vegetation canopy is mainly distributed in [0, 5) and [10, 25). Moreover, it was found that as the canopy height increaseed, the RMSE and MAE also increased, and thus were positively correlated, and as the canopy height increases, the R^2 decreases, and is thus negatively correlated. This can be explained by the fact that as the CHM value increases, the age class of the tree species increases, and the canopy cover increases. Therefore, the photon signal emitted by ICESat-2/ATLAS is more susceptible to environmental factors, and the chance of it passing through the forest canopy and the ground vegetation and then reflecting back to the photon signal receiver from the ground surface is lower and the error increases [19, 32].

Fig. 6 revealed that the median confidence interval range for the different canopy scales (zone groups) of the strong beam was narrower than that of the weak beam, and the absolute value of the ATLAS height minus the G-LiHT height was closer to zero, with higher estimation accuracy. It was also observed that the weak beam band 7 group [30, 35) had the largest year-on-year error, because of the low number and weight of canopy heights (N%) of 0.3%. The results for the band 1 group [0, 5) were relatively poor, due to the lower intensity of the weak beam laser and the canopy in this band was made up of shrub layers or dwarf trees with high vegetation cover. The photon signal received was also relatively weak, so the distance between the ground and canopy photons in the received photon signal was small. So it is more difficult for the photon classification algorithm to classify the ground and canopy photons and produced a larger error [9].

Table 3. Estimation accuracy statistics of ICESat-2/ATLAS data using different laser types.

Group Number	Canopy Height (m)	N (%)	R^2	RMSE (m)	MAE (m)
1	[0,5)	24.0/31.7	0.9980/0.9977	0.4590/0.5010	0.3224/0.3235
2	[5,10)	7.6/5.4	0.9999/0.9996	0.4000/0.5230	0.2851/0.2930
3	[10,15)	14.2/17.4	0.9994/0.9992	0.6320/0.6500	0.3349/0.3574
4	[15,20)	24.4/23.1	0.9991/0.9982	0.7120/0.7950	0.3490/0.3901
5	[20,25)	24.3/17.8	0.9987/0.9988	0.7210/0.6990	0.3308/0.3591
6	[25,30)	4.5/4.3	0.9971/0.9962	0.7580/0.5950	0.4190/0.3579
7	[30,35)	1.0/0.3	0.9952/0.9999	0.5440/0.1760	0.4091/0.2163

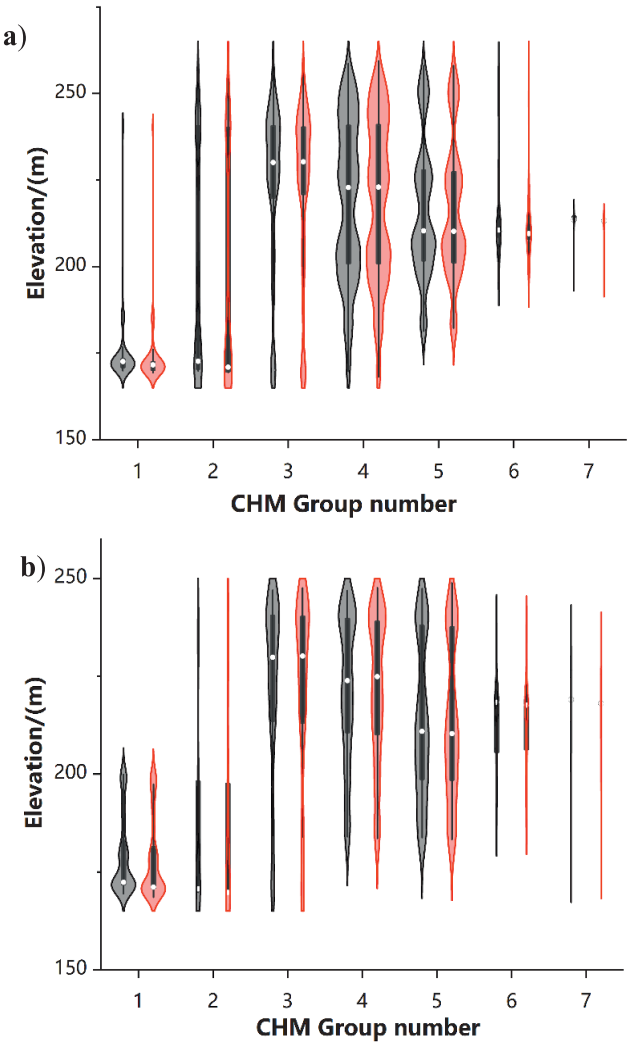

Fig. 6. a) Canopy height distribution of different groups using strong beams. b) Canopy height distri-bution of different groups using weak beams.

Optimisation of Data Processing for Satellite-Based Photon Counting Radar

The ICESAT-2/ATLAS data product has two advantages over the ICEAT-GLAS data product. Firstly, it is easier to preproce the ICESAT-2/ATLAS data product is than the ICEAT-GLAS data product, mainly in that there is no need for complicated waveform solving, and information such as quantile height can be obtained directly from the dataset, facilitating various research analyses [33]. Secondly, the enhanced intensity of the laser pulse reduces the spot diameter of ATLAS and consequently increases the spot density, which allows for finer photon point cloud data to be obtained than with GLAS. In summary, the ICESAT-2/ATLAS data product has strong advantages and application prospects, but the ICESAT-2 product data require a centralized record of all single-photon events, and each dataset contains more than 10 million photon events, i.e., a larger data volume than GLAS waveform LiDAR [22], it is difficult to use common methods for fast and efficient reading and processing. In contrast, our study proposed a Python-based visualization and processing software for the ATLAS dataset, which can perform joint processing of data products in a very short time to obtain valid photon events in the region of interest, thus reducing the difficulty of data processing. As compared with the study of Popescu, S. C. et al. from 2018, which used the MABEL dataset to simulate ICESAT-2 and obtain DTMs [17], the results show that our proposed method yields higher accuracy and fewer errors. This may be because the dataset at that time used simulated data and the piggyback platform was an aircraft, which is somewhat different from the current inorbit satellites. In addition, we used a comprehensive algorithm that has been modified by NASA several times. This is again somewhat different from the traditional point cloud denoising and filtering algorithms and photon classification algorithms, which may also be the source of the differences in errors.

We also compared our results with those of Neuenschwander, Amy et al. from 2019 who used the ATL08 product for terrain extraction in Alaska and California and concluded that terrain extraction errors were less than 2 m in mountainous regions of California and less than 1 m on the plains of Alaska [16]. This is in general accordance with the present study, but does not provide further analysis concerning the accuracy of terrain extraction at different canopy heights, which is what our study adds. We grouped the different canopy heights in the study area at 5 m levels, and then extracted the topography for the overall and grouped vegetation cover states. The ability of photon counting radar systems to detect terrain was analyzed by simulating the performance of ATLAS under different vegetation cover types. We did not choose different latitudes and longitudes with different ecological communities for the comparative study because the study environment itself is extremely variable, which is why we ultimately chose to group canopies under a uniform study area. Comparisons are only meaningful if the relative variables are uniform.

Finally, we also analyzed canopy grouping extraction using canopy photons from ATLAS, as compared to CHM from the G-LiHT airborne LiDAR, and found that the CHM from the airborne LiDAR gave a much finer map of vegetation cover. The canopy information obtained by ATLAS was therefore not utilized; the more accurate airborne LiDAR data were selected.

Transportability of Satellite-Based Photon Counting Radar in Environmental Resources

The ICESAT-2/ATLAS satellite-based photon-counting radar has gained increasing academic attention since its launch in 2018. Various data products derived from its raw data have been used in marine ecological monitoring, water resources monitoring, forest resources

monitoring, and topographic structure detection [4, 31, 34-37]. For example, the ability of ICESat-2 to detect horizontal surface depths was analyzed in 2019 using simulated MABEL data by Parrish, C.E. et al. It was demonstrated that ATLAS has a maximum depth mapping capability of nearly 1 Secchi in water depths of up to 38 m and Kd (490) in the range of 0.05-0.12 m^{-1} [28]. In 2019, Narine, Lana L. et al. developed a method to use ICESat-2 data in vegetated areas, primarily using linear regression models to investigate the ability of ICESat-2 to estimate AGB during the day and night [12]. In addition, they combined ATL08 data with Landsat data to perform a joint inversion of the AGB of southeast Texas vegetation using a random forest model. This was validated with airborne Li-DAR data and obtained good results. In 2021, Babbel B.J. et al. used the SDB from ICESat-2 to generate a bathymetric surface model and developed an efficient process with RMSEs of 0.96 and 1.54 m when using Sentinel-2 and Landsat 8 participation, respectively [38]. Overall, this shows that ICESat-2/ATLAS has great potential for future applications [39-41]. In future studies, ICESat-2/ATLAS can be combined to conduct in-depth research on the physical structure of forests, such as aboveground biomass and carbon storage in ecologically fragile regions or alpine mountainous areas, they can be used to study biochemical parameters such as vegetation LAI, nitrogen, phosphorus, and potassium in low-latitude tropical rainforest and monsoon rainforest environments, and to further analyze biochemical parameters such as nitrogen, phosphorus, and potassium in protected areas and national forest parks. This study was conducted using ICESat-2/ATLAS. This study used different ICESat-2/ATLAS laser intensities to study the detection capability of DTM at different canopy heights. This is significant for the development of more indepth investigations and has great practical significance in terms of accurately understanding the macroscopic distribution and the existing quantity of environmental resources.

Conclusions

In this study, based on Oxford County in western Maine, USA, the accuracy of the ICESat-2/ATLAS inversion of forest DTM with different laser intensities at different canopy heights was evaluated by the DTM of airborne G-LiHT. The accuracy of the inversed forest DTM is discussed in detail, and the effect of different canopy heights on the accuracy of the inverse forest DTM was explored by comparing them in canopy height groupings. The following conclusions were drawn.

1. The results show that the inversed forest DTM accuracy of strong beams is R^2 = 0.9995, RMSE = 0.6348 m, MAE = 0.3556 m; the inversed forest DTM accuracy of weak beams is R^2 = 0.9994, RMSE = 0.6584 m, MAE = 0.3816 m. The inversed forest DTM accuracy of strong beams is superior to that of weak beams, but both strong and weak beams can provide a high degree of confidence and new scientific data.
2. From the results of the canopy height grouping statistics, the data generally show that, as the canopy height changes and the tree layer depression increases, the ICESat-2/ATLAS data inversion of the understorey DTM exhibits an increase in error and a decrease in accuracy.
3. The accuracy of ICESat-2/ATLAS data for the inversion of the DTM under the tree layer is better than that of the dwarf tree and shrub layer. This is mainly due to the reduced distance between canopy photons and ground photons, which causes an increase in misclassification when using the ATL08 product algorithm.
4. In summary, the results of the study can provide an important addition to knowledge for the use of ATL03 and ATL08 data products and DEM accuracy assessment in similar areas. In future studies, we will consider generating DEM data products under different ecological environments and different community structures. It can provide a new factor for ecological assessment, geodesy.

Acknowledgments

The authors would like to thank the NASA NSIDC for distributing the ICESat-2 data (https://search.earthdata.nasa.gov, accessed on 13 January 2022), the G-LiHT data (https://glihtdata.gsfc.nasa.gov/, accessed on 20 March 2021), and the anonymous reviewers and members of the editorial team for their constructive comments.

Conflict of Interest

The authors declare no conflict of interest.

References

1. LIU M., XING Y., WU H., YOU H. Study on Mean Forest Canopy Height Estimation Based on ICESat-GLAS Waveforms. Forest Research, **27** (3), 309, **2014**.
2. MOUSSAVI M.S., ABDALATI W., SCAMBOS T., NEUENSCHWANDER A. Applicability of an automatic surface detection approach to micropulse photon-counting lidar altimetry data: implications for canopy height retrieval from future ICESat-2 data. International Journal of Remote Sensing, **35** (13), 5263, **2014**.
3. HUANG X., XIE H., LIANG T., YI D. Estimating vertical error of SRTM and map-based DEMs using ICESat altimetry data in the eastern Tibetan Plateau. International Journal of Remote Sensing, **32** (18), 5177, **2011**.
4. MA Y., LI S., ZHANG W., ZHANG Z., LIU R., WANG X.H. Theoretical ranging performance model and range walk error correction for photon-counting lidars with multiple detectors. Optics express, **26** (12), 15924, **2018**.

5. LIU Z., ZHU J., FU H., ZHOU C., ZUO T. Evaluation of the Vertical Accuracy of Open Global DEMs over Steep Terrain Regions Using ICESat Data: A Case Study over Hunan Province, China. Sensors, **20** (17), 4865, **2020**.
6. MONTESANO P.M., ROSETTE J., SUN G., NORTH P., NELSON R.F., DUBAYAH R.O., KHARUK V. The uncertainty of biomass estimates from modeled ICESat-2 returns across a boreal forest gradient. Remote Sensing of Environment, **158**, 95, **2015**.
7. NEUENSCHWANDER A., MAGRUDER L. The Potential Impact of Vertical Sampling Uncertainty on ICESat-2/ ATLAS Terrain and Canopy Height Retrievals for Multiple Ecosystems. Remote Sensing, **8** (12), 1039, **2016**.
8. NEUENSCHWANDER A.L., MAGRUDER L.A. Canopy and Terrain Height Retrievals with ICESat-2: A First Look. Remote Sensing, 1, **2019**.
9. XING Y., HUANG J., GRUEN A., QIN L. Assessing the Performance of ICESat-2/ATLAS Multi-Channel Photon Data for Estimating Ground Topography in Forested Terrain. Remote Sensing, **12** (13), 2084, **2020v**
10. MAGRUDER L., NEUMANN T., KURTZ N. ICESat-2 Early Mission Synopsis and Observatory Performance. Earth and space science (Hoboken, N.J.), **8** (5), e2020EA001555, **2021**.
11. NEUMANN T.A., MARTINO A.J., MARKUS T., BAE S., BOCK M.R., BRENNER A.C., THOMAS T.C. The Ice, Cloud, and Land Elevation Satellite – 2 mission: A global geolocated photon product derived from the Advanced Topographic Laser Altimeter System. Remote Sensing of Environment, 233, 111325 %U https://linkinghub.elsevier.com/retrieve. **2019**.
12. NARINE L.L., POPESCU S., ZHOU T., SRINIVASAN S., HARBECK K. Mapping forest aboveground biomass with a simulated ICESat-2 vegetation canopy product and Landsat data. Annals of Forest Research, **62** (1), 69, **2019**.
13. NEUENSCHWANDER A., PITTS K. The ATL08 land and vegetation product for the ICESat-2 Mission. Remote Sensing of Environment, **221**, 247, **2019**.
14. LI W., NIU Z., SHANG R., QIN Y., WANG L., CHEN H. High-resolution mapping of forest canopy height using machine learning by coupling ICESat-2 LiDAR with Sentinel-1, Sentinel-2 and Landsat-8 data. International Journal of Applied Earth Observation and Geoinformation, **92**, 102163, **2020**.
15. MARSHAK C., SIMARD M., DUNCANSON L., SILVA C.A., DENBINA M., LIAO T.-H., ARMSTON J. Regional Tropical Aboveground Biomass Mapping with L-Band Repeat-Pass Interferometric Radar, Sparse Lidar, and Multiscale Superpixels. Remote Sensing, **12** (**12**), 2048, **2020**.
16. WANG C., ZHU X., NIE S., XI X., LI D., ZHENG W., CHEN S. Ground elevation accuracy verification of ICESat-2 data: a case study in Alaska, USA. Optics express, **27** (26), 38168, **2019**.
17. POPESCU S.C., ZHOU T., NELSON R., NEUENSCHWANDE A., SHERIDAN R., NARINE L., WALSH K.M. Photon counting LiDAR: An adaptive ground and canopy height retrieval algorithm for ICESat-2 data. Remote Sensing of Environment, **208**, 154, **2018**.
18. MARKUS T., NEUMANN T., MARTINO A., ABDALATI W., BRUNT K., CSATHO B., ZWALLY J. The Ice, Cloud, and land Elevation Satellite-2 (ICESat-2): Science requirements, concept, and implementation. Remote Sensing of Environment, **190**, 260, **2017**.
19. NEUENSCHWANDER A., GUENTHER E., WHITE J.C., DUNCANSON L., MONTESANO P. Validation of ICESat-2 terrain and canopy heights in boreal forests. Remote Sensing of Environment, **251**, 112110, **2020**.
20. MA Y., LIU R., LI S., ZHANG W., YANG F., SU D. Detecting the ocean surface from the raw data of the MABEL photon-counting lidar. Optics express, **26** (19), 24752, **2018**.
21. WANG X., HOLLAND D.M., GUDMUNDSSON G.H. Accurate coastal DEM generation by merging ASTER GDEM and ICESat/GLAS data over Mertz Glacier, Antarctica. Remote Sensing of Environment, **206**, 218, **2018v**
22. SUN T., QI J., HUANG H. Discovering forest height changes based on spaceborne lidar data of ICESat-1 in 2005 and ICESat-2 in 2019: a case study in the Beijing-Tianjin-Hebei region of China. Forest Ecosystems, **7** (1), 53, **2020**.
23. HUANG J., XING Y., YOU H., QIN L., TIAN J., MA J. Particle Swarm Optimization-Based Noise Filtering Algorithm for Photon Cloud Data in Forest Area. Remote Sensing, **11** (8), 980, **2019**.
24. MA Y., XU N., LIU Z., YANG B., YANG F., WANG X.H., LI S. Satellite-derived bathymetry using the ICESat-2 lidar and Sentinel-2 imagery datasets. Remote Sensing of Environment, **250**, 112047, **2020**.
25. ZHU X., WANG C., NIE S., PAN F., XI X., HU Z. Mapping forest height using photon-counting LiDAR data and Landsat 8 OLI data: A case study in Virginia and North Carolina, USA. Ecological Indicators, **114**, 106287, **2020**.
26. HERZFELD U.C., TRANTOW T., LAWSON M., HANS J., MEDLEY G. Surface heights and crevasse morphologies of surging and fast-moving glaciers from ICESat-2 laser altimeter data - Application of the density-dimension algorithm (DDA-ice) and evaluation using airborne altimeter and Planet SkySat data. Science of Remote Sensing, **3**, 100013, **2021**.
27. NAN, FENG, LIU, LI Iterative Pointing Angle Calibration Method for the Spaceborne Photon-Counting Laser Altimeter Based on Small-Range Terrain Matching. Remote Sensing, **11** (18), 2158, **2019**.
28. PARRISH C.E., MAGRUDER L.A., NEUENSCHWANDER A.L., FORFINSKI-SARKOZI N., ALONZO M., JASINSKI M. Validation of ICESat-2 ATLAS Bathymetry and Analysis of ATLAS's Bathymetric Mapping Performance. Remote Sensing, **11** (14), 1634. **2019**.
29. GHOSH S.M., BEHERA M.D., PARAMANIK S. Canopy Height Estimation Using Sentinel Series Images through Machine Learning Models in a Mangrove Forest. Remote Sensing, **12** (9), 1519, **2020**.
30. MALAMBO L., POPESCU S.C. Assessing the agreement of ICESat-2 terrain and canopy height with airborne lidar over US ecozones. Remote Sensing of Environment, **266**, 112711, **2021**.
31. SHEN X., KE C.-Q., YU X., CAI Y., FAN Y. Evaluation of Ice, Cloud, And Land Elevation Satellite-2 (ICESat-2) land ice surface heights using Airborne Topographic Mapper (ATM) data in Antarctica. International Journal of Remote Sensing, **42** (7), 2556, **2021**.
32. SILVA C.A., DUNCANSON L., HANCOCK S., NEUENSCHWANDER A., THOMAS N., HOFTON M., DUBAYAH R. Fusing simulated GEDI, ICESat-2 and NISAR data for regional aboveground biomass mapping. Remote Sensing of Environment, **253**, 112234, **2021**.
33. GLEASON A.C.R., SMITH R., PURKIS S.J., GOODRICH K., DEMPSEY A., MANTERO A. The Prospect of Global

Coral Reef Bathymetry by Combining Ice, Cloud, and Land Elevation Satellite-2 Altimetry With Multispectral Satellite Imagery. Frontiers in Marine Science, **8**, 694783, **2021**.
34. O'LOUGHLIN F.E., PAIVA R.C.D., DURAND M., ALSDORF D.E., BATES P.D. A multi-sensor approach towards a global vegetation corrected SRTM DEM product. Remote Sensing of Environment, **182**, 49, **2016**.
35. CHEN B., PANG Y., LI Z., NORTH P., ROSETTE J., SUN G., LU H. Potential of Forest Parameter Estimation Using Metrics from Photon Counting LiDAR Data in Howland Research Forest. Remote Sensing, **11** (7), 856, **2019**.
36. DUNCANSO L., NEUENSCHWANDER A., HANCOCK S., THOMAS N., FATOYINBO T., SIMARD M., DUBAYAH R. Biomass estimation from simulated GEDI, ICESat-2 and NISAR across environmental gradients in Sonoma County, California. Remote Sensing of Environment, **242**, 111779, **2020**.
37. QUEINNEC M., WHITE J.C., COOPS N.C. Comparing airborne and spaceborne photon-counting LiDAR canopy structural estimates across different boreal forest types. Remote Sensing of Environment, **262**, 112510, **2021**.
38. BABBEL B.J., PARRISH C.E., MAGRUDER L.A. ICESat-2 Elevation Retrievals in Support of Satellite-Derived Bathymetry for Global Science Applications. Geophysical research letters, **48** (5), e2020GL090629, **2021**.
39. YUAN C., GONG P., BAI Y. Performance Assessment of ICESat-2 Laser Altimeter Data for Water-Level Measurement over Lakes and Reservoirs in China. Remote Sensing, **12** (5), 770, **2020**.
40. LUO S., SONG C., ZHAN P., LIU K., CHEN T., LI W., KE L. Refined estimation of lake water level and storage changes on the Tibetan Plateau from ICESat/ICESat-2. Catena, **200**, 105177. **2021**.
41. XIANG J., LI H., ZHAO J., CAI X., LI P. Inland water level measurement from spaceborne laser altimetry: Validation and comparison of three missions over the Great Lakes and lower Mississippi River. Journal of Hydrology (Amsterdam), **597**, 126312. **2021**.
42. NIE S., WANG C., XI X., LUO S., LI G., TIAN J., WANG H. Estimating the vegetation canopy height using micro-pulse photon-counting LiDAR data. Optics express, **26** (10), A520, **2018**.